Meteoritics & Planetary Science 41, Nr 10, 1539–1550 (2006)
Abstract available online at http://meteoritics.org

An atmospheric blast/thermal model for the formation of high-latitude pedestal craters

Kelly WROBEL[1*], Peter SCHULTZ[1], and David CRAWFORD[2]

[1]Department of Geological Sciences, Brown University, Box 1846, Providence, Rhode Island 02912, USA
[2]Sandia National Laboratories, P. O. Box 5800, MS 0836, Albuquerque, New Mexico 87185, USA
[*]Corresponding author. E-mail: kelly_wrobel@brown.edu

(Received 15 October 2005; revision accepted 17 April 2006)

Abstract–Although tenuous, the atmosphere of Mars affects the evolution of impact-generated vapor. Early-time vapor from a vertical impact expands symmetrically, directly transferring a small percentage of the initial kinetic energy of impact to the atmosphere. This energy, in turn, induces a hemispherical shock wave that propagates outward as an intense airblast (due to high-speed expansion of vapor) followed by a thermal pulse of extreme atmospheric temperatures (from thermal energy of expansion). This study models the atmospheric response to such early-time energy coupling using the CTH hydrocode written at Sandia National Laboratories. Results show that the surface surrounding a 10 km diameter crater (6 km "apparent" diameter) on Mars will be subjected to intense winds (~200 m/s) and extreme atmospheric temperatures. These elevated temperatures are sufficient to melt subsurface volatiles at a depth of several centimeters for an ice-rich substrate. Ensuing surface signatures extend to distal locations (~4 apparent crater diameters for a case of 0.1% energy coupling) and include striations, thermally armored surfaces, and/or ejecta pedestals—all of which are exhibited surrounding the freshest high-latitude craters on Mars. The combined effects of the atmospheric blast and thermal pulse, resulting in the generation of a crater-centered erosion-resistant armored surface, thus provide a new, very plausible formation model for high-latitude Martian pedestal craters.

INTRODUCTION AND BACKGROUND

"Pedestal craters" as defined here represent a class of impact crater unique to Mars and distinguishable by their distinct form: craters perched near the center of a mesa or plateau surrounded by an outward-facing scarp. They represent relics where the substrate in which the crater had formed was eroded away (see Arvidson et al. 1979; Mouginis-Mark 1987; Schultz and Lutz 1988; Barlow 2005). This nearly complete removal of the target substrate, along with the concentration of recent examples of pedestal craters at high latitudes within circumpolar mantling deposits, has prompted the suggestion that some process occurring during their formation must act to preserve or protect a volatile-rich substrate (Schultz 1988b; Schultz and Lutz 1988; Tanaka 2000).

Distal terrains around the freshest high-latitude craters on Mars are striated (with terminal lobes) and extend to distances similar to the maximum pedestal diameters (~10 crater diameters, see Fig. 1). Here we explore the possibility that such features are the consequence of early-time atmospheric effects on the impact process (passage of a shock blast and intense heating). The resulting modification of the surface by these effects induces armoring previously recognized as necessary for the future development of pedestal craters (see Arvidson et al. 1976, 1979).

Atmospheric responses to an impact can be separated into early- and late-time processes, with subsequent effects ranging from slight winds to global catastrophe (Jones and Kodis 1982; Schultz and Gault 1990; Schultz 1992; Adushkin and Nemchinov 1994). Early-time interactions result from energy directly coupled to the atmosphere prior to and just after impact (compression stage), whereas late-time interactions involve the atmospheric response to crater growth (excavation and ejection). Many studies have focused on late-time atmospheric responses to indirect energy coupling, such as winds and turbulence caused by the outward-moving ejecta curtain, frictional drag, etc. (e.g., Schultz and Gault 1979, 1982; Schultz 1992a, 1996; Barnouin-Jha and Schultz 1996, 1998), in great detail. The present study focuses on the early-time direct transfer of energy to an atmosphere via the expansion of an impact-induced vapor (e.g., O'Keefe and Ahrens 1982; Ahrens and O'Keefe 1987; Roddy et al. 1987; Schultz 1988b, 1996;

© The Meteoritical Society, 2006. Printed in USA.

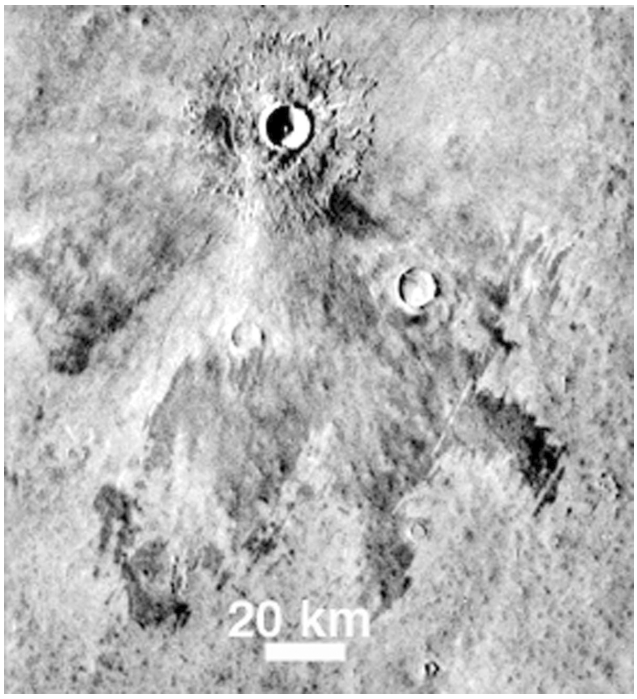

Fig. 1. Image of a fresh, high-latitude (located at approximately 73°N, 320°W) pre-pedestal crater ~12 km in diameter on Mars. Scouring of the surface extends to ~8 crater diameters.

Nemtchinov et al. 2002). The results presented in the remainder of this paper thus address only one specific aspect of an atmospheric response.

The range in possible interactions between an atmosphere and the impact process make the depiction of a "complete picture" very complex. Before integrating into a "complete picture," each type of atmospheric response needs to be understood. The present study is a first step to addressing distal surface signatures resulting from the response to early-time vapor expanding into an atmosphere. Such an approach provides a basis for recognizing signatures of potential near-surface volatiles.

Impact-Generated Vapor

Impact-induced vaporization is a key component of early-time cratering and a widely studied phenomenon. Previous studies, both experimental (e.g., Schultz 1996; Sugita et al. 1998; Wrobel et al. 2004) and computational (e.g., Adushkin and Nemchinov 1994; Pierazzo and Melosh 1999), focused on the generation and expansion of vapor clouds in an attempt to better understand impact vaporization. At least four different components of impact-generated vapor have been distinguished: vapor associated with the jetting phase, a downrange-moving vapor cloud, a plume that expands above impact, and a later-time cloud that evolves from the redirection of vapor temporarily contained in the penetration cavity (Schultz 1996). This work will only address the early-time plume that expands symmetrically above impact, neglecting the role of the shock wave associated with the incoming impactor. The effects due to atmospheric interactions with other vapor will be treated in a later contribution.

MODELING STRATEGIES

The direct transfer of energy to an atmosphere from an expanding impact vapor results in a hemispherical shock wave that propagates outward as an intense airblast. The effects of such an airblast and the ensuing surface signatures are dependent on the initial ambient atmospheric and surface conditions. For example, the thick atmosphere of Venus provides a unique environment where the impact-induced vapor is not able to expand to great distances. As a result, extreme interactions with the atmosphere induce distinctive surface signatures relatively close to the crater (Schultz 1992b; Sugita and Schultz 2002). On Mars, the present-day tenuous atmosphere cannot restrain an expanding vapor cloud; consequently, the effects of atmospheric interactions extend to large distances.

Analytical calculations derived from explosion physics (Taylor 1950a, 1950b; Sedov 1959) provide a relatively straightforward approach for describing an expanding shock front (airblast). The response of an atmosphere to energy imparted by early-time impact vapor has been previously examined using these analytically derived expressions (Schultz 1988b, 1992b). These studies showed that while an instantaneous surface explosion is fundamentally different from an impact by a hypervelocity projectile, the classic blast wave solution by Taylor (1950a) does provide a reasonable first-order approximation for benchmark purposes:

$$R = S(\gamma) t^{2/5} E_A^{1/5} \rho_o^{-1/5} \quad (1)$$

where R denotes the radius of the spherically expanding shock front generated by an explosion of energy E_A, $S(\gamma)$ is a function of the ratio γ of the specific heats of the surrounding atmosphere (~1.3 for CO_2, i.e. the Martian atmosphere), t measures the time since explosion, and ρ_o is the ambient atmospheric density.

Point-source approximations for impact cratering evolved from studies of explosion cratering. A point-source model is often used to approximate the effects of energy deposition in the target during an impact (e.g., Holsapple and Schmidt 1987). Similarly, the transfer of energy from a planetary impact to a surrounding atmosphere can be modeled with an assumption of an instantaneous point-source release of a large amount of energy into a small volume of gas. The resulting shock physics can be characterized well using the analytical solutions from explosion cratering as described above (Taylor 1950a, 1950b; Sedov 1959). Such an approach provides useful first-order results but also makes simplifying assumptions and neglects the complex interactions that occur during the impact process.

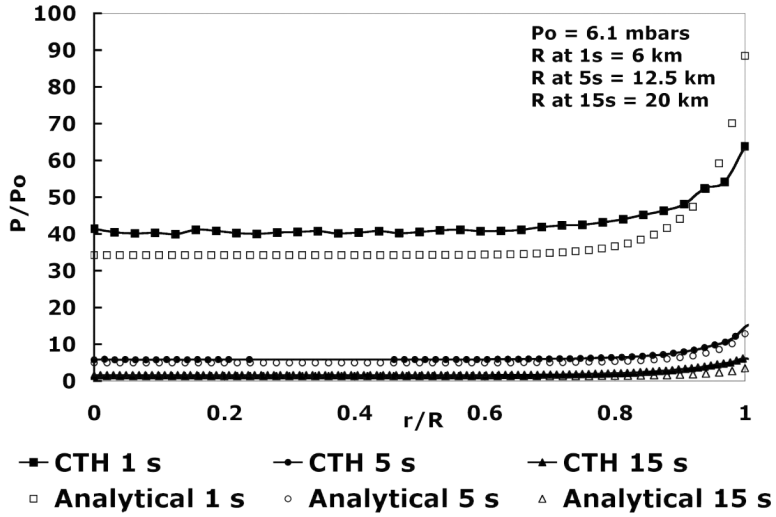

Fig. 2. Comparison between analytical calculations made from the classic blast wave solution (Equation 1) by Taylor (1950a) and computational modeling (CTH) results from a point-source explosion into the Martian atmosphere. *R* indicates the position of the shock front and *Po* is the ambient atmospheric pressure (610 Pa). *P* denotes the atmospheric pressure at a distance *r* ($r < R$) from the source region. Energy inputted into the model is 0.1% of the initial kinetic energy required to produce a crater 10 km in diameter on Mars.

In order to appreciate such differences and to validate the general results obtained, this study involves a combination of two different computational models: a point-source energy release model (deposition into a Martian atmosphere) and a Martian impact model. Both models employ the CTH hydrocode, a multidimensional, multi-material shock physics analysis package developed at Sandia National Laboratories (McGlaun et al. 1990). The point-source model is a clear-cut computational simulation with results that are easily comparable to analytical calculations. It supplies a first-order estimate of the atmospheric response to early-time impact energy coupling that can be used as a benchmark for interpreting the more complex results of the full-up impact model.

CTH simulations of impacts on Mars have previously been modeled for various scientific studies (e.g., Stewart et al. 2004). Here the focus is only on the atmospheric response to the deposition of energy from expanding impact-induced vapor. In such simulations, however, it is nearly impossible to single out which specific responses are due to just the vapor component. Thus it is useful to compare the results of the Martian impact simulation with those from the point-source energy model in an attempt to isolate the conditions being induced solely from the early-time symmetrically expanding vapor.

Point-Source Energy Model

The first of the two CTH simulations presented in this study involves a point-source instantaneous release of a large amount of energy into the ambient Martian atmosphere. It is a two-dimensional axisymmetric model that incorporates the adaptive mesh refinement approach (Crawford et al. 2002) in order to provide high-resolution conditions along the resulting shock blast front. For this simulation, the atmosphere was composed of CO_2 gas (modeled as a user-defined ideal gas, $\gamma = 1.3$) under ambient Martian conditions (density of 1.55e-5 g/cc and temperature of ~240 K near the surface).

For this model, the energy coupled to the atmosphere was assumed to be a small percentage (0.1%) of the total energy from an asteroid 1 km in diameter impacting at 12 km/s (~10^{23} ergs). The fraction of energy actually transferred to an atmosphere via impact vapor expansion remains uncertain, ranging anywhere from ~0.01% to ~50% (dry-ice target), and depends on many factors such as impact angle, impact velocity, and surface and atmospheric conditions (Schultz 1996). This coupling energy can be determined post-impact, however, using the limits of vapor cloud expansion and Taylor's blast wave equation (Equation 1). The estimate used here is a conservative one based on such previous approximations (Schultz 1992b) and direct measurements from laboratory experiments (Schultz 1996).

Analytical calculations (Equation 1) provide a reality check for the results of this point-source hydrocode model. Fig. 2 reveals the good correlation between the two approaches. It should be noted, however, that Taylor's solution is primarily applicable only to conditions for a strong shock (when $P_{wave} >> P_{ambient}$). The CTH hydrocode, however, tracks the transition from a strong to weak shock regime. Differences between the analytical and the CTH results (as seen in Fig. 2) due to this simplification are not substantial enough, however, to preclude using Taylor's solution for first-glance validation of the point-source energy model.

Martian Impact Model

CTH impact simulations reveal the atmospheric response to an impact in much greater detail than is possible with a point-source approximation. The second computational model of this study thus involves a 12 km/s vertical impact of a 1 km diameter dunite projectile into a volatile-rich target with an atmosphere under ambient Martian conditions (same atmospheric conditions as applied in the point-source energy model). The SESAME equation of state package was used to model the projectile and target, which consisted of a 500 m layer of water ice (40% porosity) overlying basalt. As in the first model, the impact simulations were run in two dimensions applying axisymmetry and the adaptive mesh refinement approach (Crawford et al. 2002) for higher resolution along the atmospheric blast front.

Gravity-scaling relations (Schmidt and Holsapple 1982; Schultz and Gault 1985) predict that an asteroid 1 km in diameter impacting at 12 km/s would produce a transient crater 6 km in diameter. The diameter in this case refers to the "apparent" transient diameter referenced to the preimpact surface, as is commonly done for experiments and computational codes. The rim-to-rim transient crater diameter, however, is 25% larger than the apparent diameter. In addition, a crater of this size on Mars should collapse, resulting in an even further enlargement by another 25% (Croft 1985; Schultz 1988a). Consequently, the conditions modeled for the present study would produce a 10 km final rim-to-rim crater diameter on Mars.

The impact simulations presented here assume a vertical impact with the projectile starting very near to the target surface, thereby neglecting the details of atmospheric entry and interaction before impact. The model was set up this way for ease of computation and interpretation of the results. The effects of impact angle and projectile wake would add another dimension of detail that will be considered in a future contribution. The current results should nevertheless apply for impact angles of 30° and higher. At these angles, experiments (Schultz 1996) and hydrocodes (Pierazzo and Melosh 1999) show the existence of an early-time vapor cloud evolving above the crater, in addition to a fast moving vapor plume that travels rapidly downrange and decouples from the excavation process. The component of vapor that remains expanding above impact, as modeled in this study, thus provides only a fraction of the total energy that is directly transferred to the atmosphere. This is consistent with the use of a conservative value of 0.1% of the initial impact energy coupled to the atmosphere in the point-source energy release simulation.

Adushkin and Nemchinov (1994) previously studied the atmospheric response to energy coupling for impacts on Earth. The results of that work provide a useful reference for comparisons with the impact model presented here (when also applied to terrestrial conditions). Results from the two studies correlate well (maximum difference of 20% in atmospheric temperature at the surface). Differences can be primarily attributed to the neglect of radiation flux in the current study. Other disparities between the two studies are related to the effects of projectile wake, also neglected here. Such wake effects are transitory, though, and minor relative to vapor expansion, primarily affecting the atmospheric column at high altitudes (Schultz 1992b, 1996).

In summary, our model is the first step in describing the temperature/pressure environment around a modest size impact on Mars for angles higher than ~30°. Neglecting the effects of both trajectory and the preimpact wake will limit detailed comparisons but will not invalidate our primary focus: the possible consequences of impact-induced atmospheric winds and extreme temperatures in regards to the melting of near-surface ices and the formation of pedestal craters.

RESULTS: POINT-SOURCE MODEL

Based on previous analytical, point-source models, if 0.1% of the initial energy of an impact is directly transferred to the Martian atmosphere, then the pressure in the resulting shock front equilibrates to ambient values when it reaches ~4 crater diameters from impact (Schultz 1992b). Results from the present CTH point-source energy simulation agree well, showing a pressure blast that extends out to ~4.2 apparent crater diameters, or ~25 km from the explosion (reached at ~50 s).

The simulation results for the range and time of shock front equilibration to ambient pressure are shown in Fig. 3. Locations closer to the energy source experience a more intense pressure blast while greater distances (beyond 25 km) are subjected to remnant effects as the atmosphere recovers (extending out to ~35 km, as seen in Fig. 3).

The plots in Fig. 3 also reveal that early-time atmospheric energy coupling generates both a rapidly moving blast wave and a large temperature pulse. Winds induced by this atmospheric blast exceed 200 m/s even out to distances of ~10 km, or ~1.5 apparent crater diameters. Recovery winds, also close to 200 m/s in magnitude, affect surfaces out to ~6 apparent crater diameters, or ~35 km (see Fig. 3a), and linger for minutes (see Fig. 3b).

Close to the initial energy source (e.g., ~2 apparent crater diameters or ~12 km from energy release), residual temperatures behind these winds remain near 1000 K after ~50 s. Farther away, however, atmospheric temperatures at the surface drop (e.g., ~500 K at ~3 apparent crater diameters), reaching a minimum of ~270 K at a range of 25 km (see Figs. 3c and 3d).

These results, while informative, are not nearly complete. Tracking the evolving conditions in the atmosphere due to the expanding vapor phases requires detailed Martian impact simulations, as presented below.

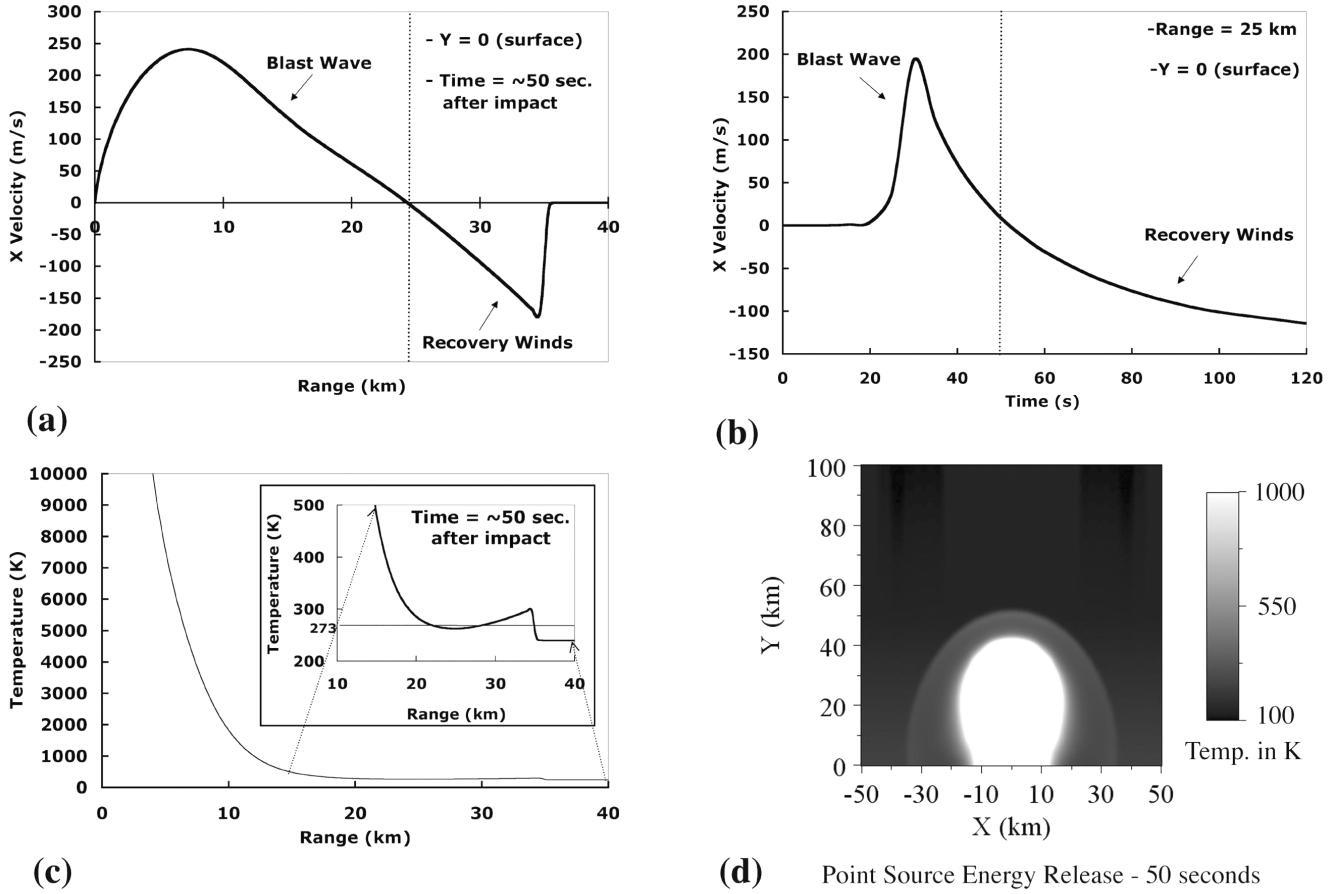

Fig. 3. CTH simulation results from the point-source energy release model. a) Horizontal velocity of atmospheric blast-induced winds (m/s) at the planetary surface as a function of range (km) at ~50 s after energy release. b) Corresponding plot to Fig. 3a: Horizontal velocity (m/s) of atmospheric winds at the surface as a function of time (s) for the location of 25 km from the energy source. The pressure in the blast front equilibrates to ambient atmospheric values once it reaches ~25 km from the explosion, which occurs at ~50 s (X velocity = 0). c) Atmospheric temperatures (K) at the surface as a function of range (km) at ~50 s after energy release. Inset shows the temperatures from 10 km to 40 km (~1.5 to ~6.5 apparent crater diameters). Ambient atmospheric temperature used was 240 K (near the surface). d) CTH simulation plot of temperature (K) for 50 s after energy release. Black denotes temperatures of 100 K or less, while white denotes temperatures of 1000 K or greater.

RESULTS: IMPACT MODEL

Pressure/Blast Wave

The CTH impact model results also document the generation of an intense pressure wave (Fig. 4). The strength of this wave corresponds rather well with the magnitude of the pressure front observed in the point-source energy model (see Fig. 2). It therefore appears that the impact calculation is capturing effects due to early-time energy deposition.

The shape and form of the impact vapor-induced pressure wave, however, differ from those produced by the point-source energy release, due to the added complexities of the impact model (such as the actual inclusion of expanding vapor). The resulting atmospheric blast does not spread uniformly outward from a point-source location. A distinction of particular importance is the noticeable coupling behavior revealed in the impact simulation results (see Fig. 4d). A high-pressure region becomes "attached" to the surface, moving outward slowly to great distances (lasting ~80 s out to ~50 km from impact). This attached region results from early-time vapor being located above the surface, not at the surface as in the point-source energy release simulation. In the impact model, the vapor is contained within the impact cavity at very early times. Eventually, it breaks away, moving up out of the cavity so that the center of mass of the cloud is now located above the surface, and then expands outward in all directions (Schultz 1996). This, in turn, results in vapor that rapidly travels downward around the lip of the cavity, into atmosphere of much lower pressure (ambient), and "attaches" to the surface (due to the continual feeding of vapor to this region as the cloud expands). This same phenomenon has been observed computationally (e.g., Crawford et al. 1995; Rybakov et al. 1997; Sugita and Schultz 2002) and in laboratory experiments from high-speed imaging of impact-generated vaporization (Schultz 1996).

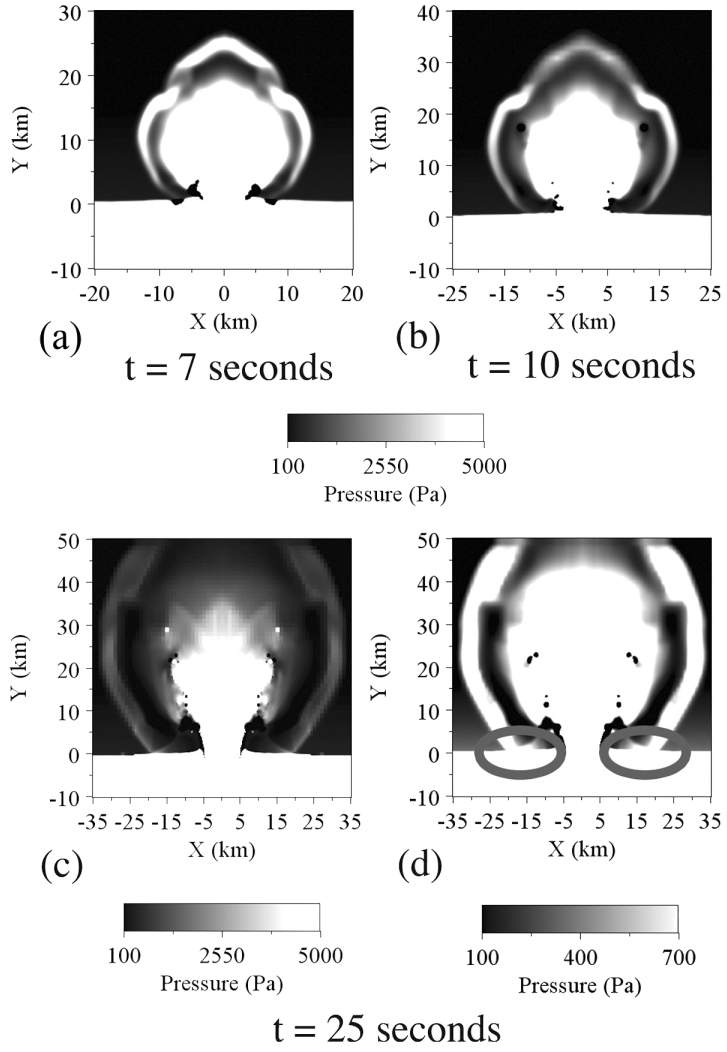

Fig. 4. Pressure plots (in Pa) from a CTH simulation of a vertical impact of a 1 km diameter dunite projectile into a 500 m layer of water ice overlying basalt surrounded by a Martian atmosphere. Figures 4a–c show the progression of the resulting pressure front with time (7 s, 10 s, and 25 s after impact) where black denotes pressures of 100 Pa or less and white represents pressures of 5000 Pa or greater. The *x* and *y* ranges of the plots increase with time in order to clearly demonstrate the extent of the results. Figure 4d again shows pressure at 25 s after impact but for a smaller span of values (white now denotes pressures of 700 Pa and greater). This plot is provided to highlight the region of high pressure that becomes coupled to the surface (circled on image).

Also unlike what was observed from the point-source model, atmospheric blast effects do not just dissipate with increasing time and distance. Figure 5 contains a series of plots showing the horizontal velocity magnitude (m/s) of blast-induced winds (for 25 s and 80 s after impact). The absolute magnitude of the velocities is used for ease in portraying the carrying capabilities of these winds. Wind direction is not important for the sake of our conclusions.

At 25 s after impact, the strongest winds are located high in the atmosphere (e.g., ~1000 m/s and greater at 8 km and above). At the same time, the surface close to the crater (within ~1 apparent crater diameter) is being subjected to winds, reaching ~175 m/s in magnitude, that are generated from the expansion of later-time vapor components (see Figs. 5a–c). The early-time symmetrically expanding vapor blasts by these proximal locations at much earlier times (as it rises out of the cavity), enforcing winds near 800 m/s.

In addition to this fast, initial blast, the region of coupled vapor produces enhanced wind velocities near the surface as it travels outward to greater distances. Figure 5c plots the magnitude of the horizontal wind velocity at the planetary surface, showing an increase at the range of vapor coupling (~25 m/s at ~23 km from impact at 25 s). The atmosphere right above the surface (at ~1 km up, again at ~23 km and 25 s) experiences more complete effects of the coupled vapor expansion, containing winds of ~300 m/s (Fig. 5b).

At later times, the combination of persistent winds from the initial blast (outward), particularly those from the lingering coupled vapor, and its recovery (inward) creates chaotic, turbulent eddies moving at hundreds of meters per

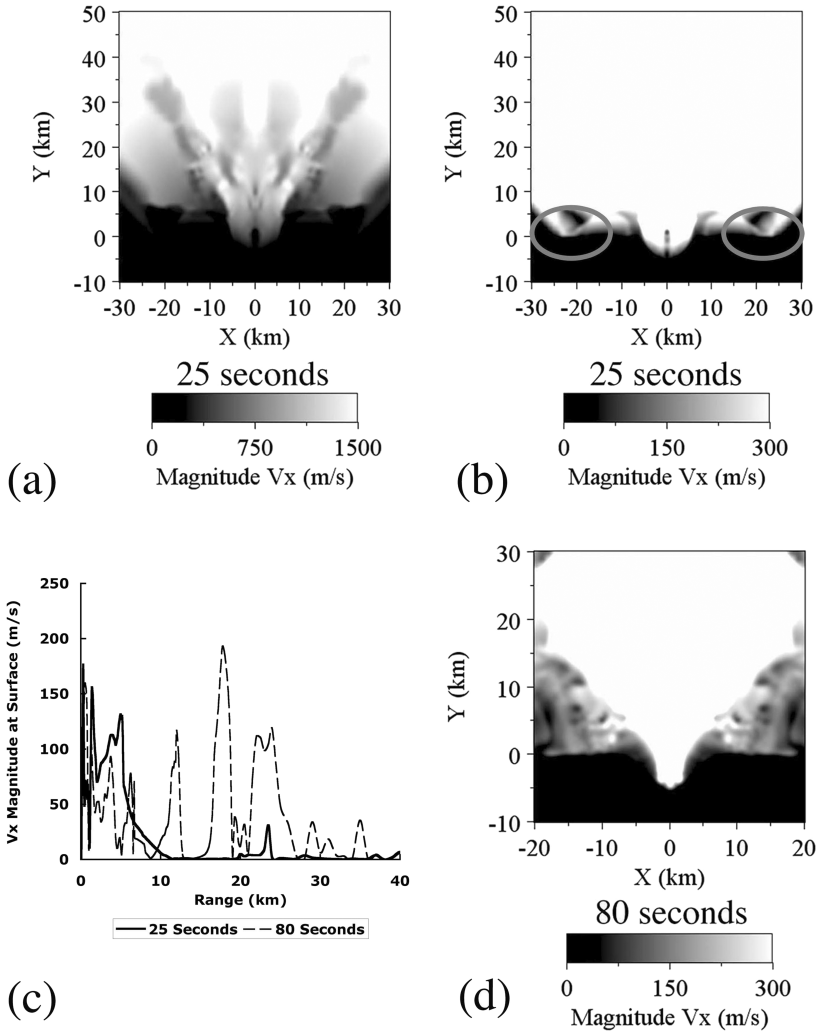

Fig. 5. Plots of horizontal velocity magnitude (absolute value, in m/s), *VXmag*, of winds generated from an early-time atmospheric blast (CTH impact model results). a) Image of *VXmag* 25 s after impact, ranging 60 km in both *x* and *y*. Black represents stationary material whereas white denotes anything moving at 1500 m/s or faster. b) Companion image to Fig. 5a. The range of velocities spans from 0 m/s (black) to 300 m/s and greater (white). c) *VXmag* at the planetary surface as a function of distance from the crater center (km) for 25 s (solid line) and 80 s (dashed line) after impact. d) Plot of *VXmag*, ranging 40 km in both *x* and *y*, at 80 s after impact. Like Fig. 5b, *VXmag* ranges from 0 m/s (black) to 300 m/s and greater (white).

second, even at a minute and a half after impact (see Figs. 5c and 5d).

Thermal Response

The point-source energy release simulation indicated that an atmosphere with lingering extreme temperatures would engulf the surface, thereby elevating subsurface temperatures during an impact. Such intense atmospheric temperatures at the surface are not present, however, in the more complete impact simulation. Instead, the expanding vapor component behind the advancing shock front transfers its heat to the surface through the "attached" vapor (highlighted in Fig. 6a). Though not as extreme as a thermally enhanced atmosphere (point-source model, Fig. 6b), this coupled region of vapor induces temperatures over 500 K, sustained for tens of seconds at a given location. At higher altitudes, the thermal wave exceeds 1000 K (sustained for minutes at ~25 km altitude) and encloses a cooler thermal bubble with temperatures around 450 K (Fig. 6a).

OBSERVATIONS/DISCUSSION

The relative complexity of the impact process, in contrast to an instantaneous explosion, makes comparisons between the two models difficult. First-glance comparisons reveal that the atmospheric response due to early-time energy transfer can be observed in impact simulations. But evaluating the magnitude of the results of the two models (strength of winds, intensity of heating) is not straightforward due to the

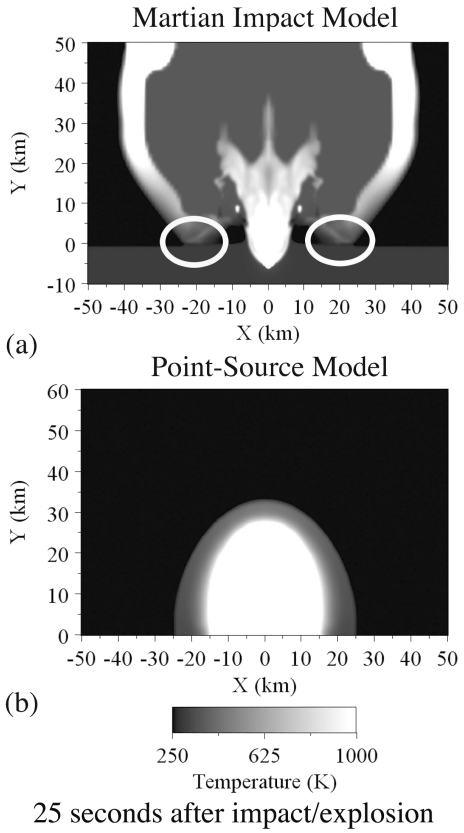

Fig. 6. Temperature (K) plots from (a) a CTH Martian impact model and (b) a CTH point-source energy release model. Images are for 25 s after impact/explosion and range 100 km in *x*, 60 km in *y*. Black represents temperatures of 250 K or less while white designates temperatures of 1000 K or greater.

inclusion of vapor expansion in the impact model. Moreover, the mechanism for heat transfer to the surface differs between the two models, due to contrasting methods (and possibly extent) of energy coupling. In the point-source model, the atmosphere heats the surface; in the impact model, the hot vapor engulfs the surface.

Despite the intricacies of the impact model, a few observations can be made exclusively from its results. For example, target porosity seems to play a significant role in the effects of atmospheric energy coupling. The magnitude of the atmospheric response is directly related to the porosity of the target with a more porous target (40% porosity versus 20% porosity) being subjected to slightly stronger winds and a larger, longer-lasting temperature pulse (see Fig. 7). On the contrary, a simulation of an impact into solid ice displayed very little atmospheric interactions due to minimal energy transfer from minimal early-time vaporization.

Atmospheric Blast Winds

The critical threshold wind speed for raising dust a few microns in diameter on Mars ranges from tens to hundreds of meters per second (Greeley et al. 1992). Consequently, the atmospheric blast-induced winds observed in the present impact model would be powerful enough to "precondition" a surface by stripping loose soil and dust well in advance of ballistic (and nonballistic) ejecta emplacement. The intensity of these winds will eventually decay at large distances (starting at ~4 apparent crater diameters from impact). Suspended material will be deposited once wind velocities fall below threshold, perhaps forming the distal lobes observed for fresh high-latitude craters on Mars (see Fig. 1). It is most likely that the finest fraction of dust (micron size) will continue to be sustained by weaker winds and eventually mixed in with ejecta that will be later deposited on the pre-conditioned surface.

Thermal Response

Figure 6a shows that atmospheric temperatures near the surface will be well above melting at the region of coupled impact vapor. Even at a minute after impact, surface temperatures are sustained at values ranging from ~300–350 K at distances of ~35–40 km from impact (Fig. 7b). Such temperatures would be sufficient to melt subsurface volatiles at a few centimeters in depth, based on a model by Paterson (1994):

$$T(z) = T(g) + T(o)e^{(-z/z^*)}\sin\{[(2\pi t)/P] - (z/z^*)\} \quad (2)$$

where

$$T(g) = T(s) + Qz/k \quad (3)$$

and $T(s)$ is the average surface temperature, Q denotes the geothermal heat and k symbolizes the thermal conductivity. $T(o)$ represents the half amplitude of temperature oscillation, P is the period of oscillation, and z^* derives from:

$$z^* = (\kappa P/\pi)^{-1/2} \quad (4)$$

where κ symbolizes the thermal diffusivity.

Geotherms calculated from Equation 2 are plotted in Fig. 8 for ice-rich and fine dust substrates. Included are geotherms from ambient Martian conditions as well as geotherms incorporating the extra heat stemming from the engulfing hot vapor. It is evident that lingering temperatures at ~30 s after the passage of the thermal pulse are high enough to produce a thermal wave extending to depths of several centimeters (temperatures above melting down to ~15 cm) at ~4 apparent crater diameters from impact for an ice-rich substrate. Consequently, if given enough time, temperatures will be sufficient to melt any ice present in the upper layers of a subsurface. Subsequent burial by ejecta will provide an insulating layer that would perhaps sustain this condition.

Nemtchinov et al. (1994) proposed that impacts of small bodies result in the formation of a heated ground layer due to absorption of thermal radiation emitted from the hot

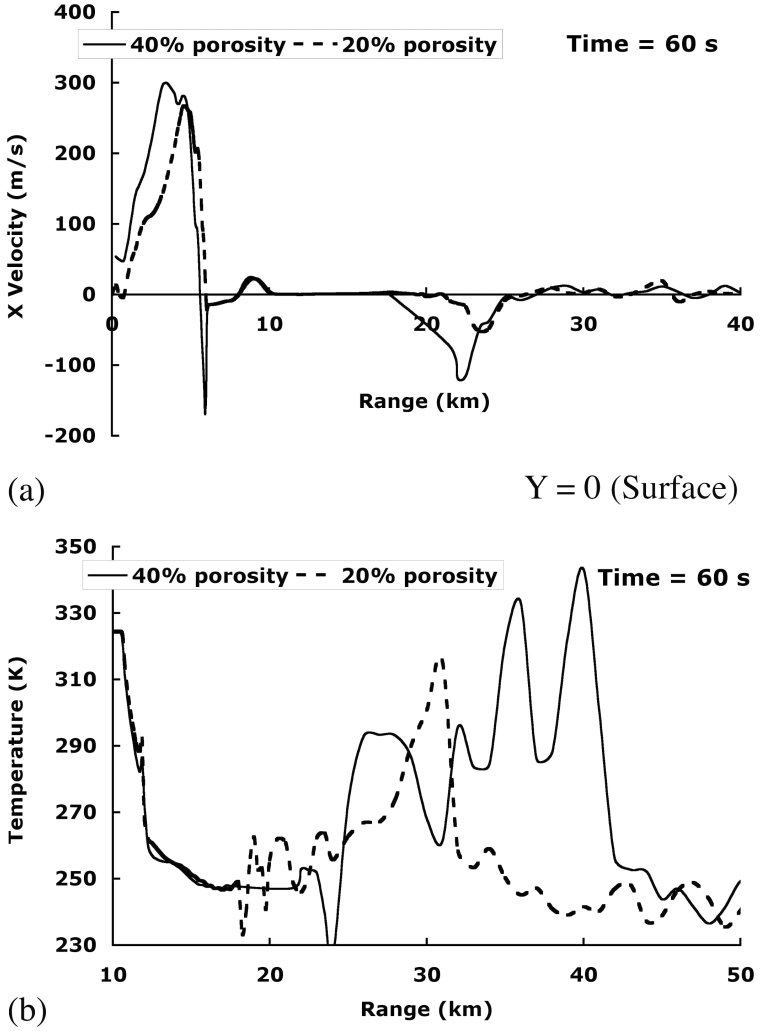

Fig. 7. Plots illustrating target porosity effects on the early-time atmospheric response (wind blast/temperature pulse) to an impact into a 500 m layer of water ice (20% and 40% porous) overlying basalt (CTH impact model results). Dashed lines represent the 20% porosity simulation and solid lines denote the simulation with a 40% porous target. a) Horizontal velocity (m/s) of atmospheric blast-induced winds at the surface as a function of range (km) from crater center at 60 s after impact. b) Temperature (K) at the surface versus range (km) at 60 s. Distances close to the crater are ignored due to extreme temperatures within the crater cavity at these locations (see Fig. 6a).

atmosphere. Additional surface/subsurface heating should thus occur in the present model due to elevated temperatures higher in the atmosphere, as shown in Fig. 6. For example, temperatures at ~5 km above the surface are sustained at ~600 K for ~20 s after passage of the thermal wave (out to distances of ~3 apparent crater diameters) and should therefore significantly affect the surface through radiative transfer. Such radiative effects, however, were not included in this model but can be approximated from the relation:

$$Q = \Psi\{E_a/[4(\pi r^2 + z_o^2)]\}\eta \quad (5)$$

where Q is the energy delivered to the unit surface, Ψ symbolizes the coefficient of conversion of the atmospheric energy into thermal radiation, E_a denotes the energy of the airblast proportional to the initial kinetic energy of the body, r is the range from impact, z_o stands for the effective height of the emitting volume, and η denotes the transmittance (Adushkin and Nemchinov 1994). Estimates using Equation 5 yield a radiation flux of ~10 kW/cm^2 or greater for the first ten seconds after impact (extending to distances of ~0.5 apparent crater diameter). Surfaces subjected to such heat will reach the evaporation limit, initiating vaporization of any present water-ice (Rybakov et al. 1997). The flux of radiation decreases to ~0.7 kW/cm^2 at later times and greater distances from impact (e.g., ~4 apparent crater diameters at ~30 s).

It is thus apparent that extreme atmospheric temperatures (both near the surface, coupled zone, and from higher altitudes, radiation) induced by early-time vapor expansion should significantly heat the substrates surrounding high-latitude craters on Mars. Considerable effects would extend to ~10 final crater diameters. It is important to note, however,

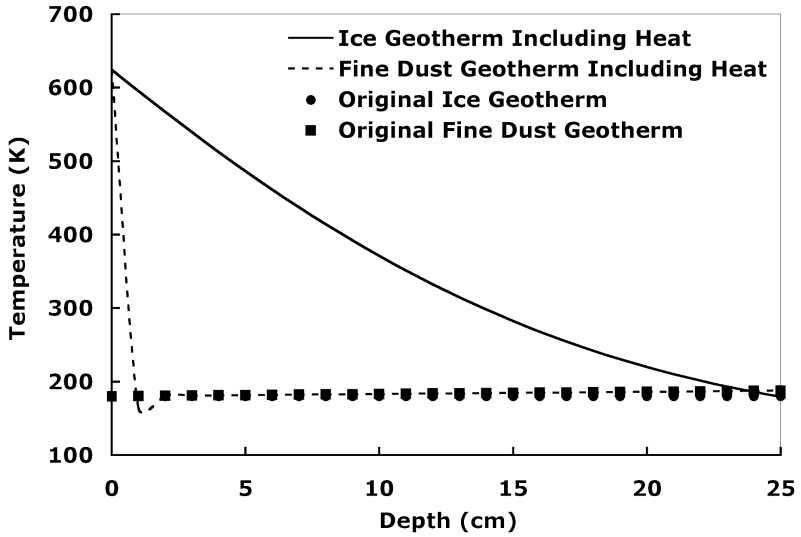

Fig. 8. Temperature (K), calculated from Equation 2, as a function of depth (cm) below the surface at 30 s after the passage of the thermal pulse. The lingering atmospheric temperatures near the surface result in a thermal wave that travels down into the upper surface layers. Comparisons between normal geotherms (for both ice and fine dust substrates) and geotherms including this extra heat source are shown for the location of ~4 apparent crater diameters.

that such effects result from the earliest stages of impact and will be overprinted closer to the crater (~2–3 crater diameters) by the later ejecta emplacement.

IMPLICATIONS

Impact-generated vaporization affects the Martian atmosphere in two ways: first, it creates a wind blast that strips away surface fines and second, it induces elevated temperatures that should melt near-surface volatiles (particularly at the coupled vapor region). High-latitude regions, covered by an ice-rich mantle and affected by seasonable mantling and orbital forcing over long time periods (e.g., Mustard et al. 2001), should be particularly sensitive to these two effects. Some possible residual surface signatures that might be found in such areas include: scoured zones (characterized by radial striations and muting of surface detail), greater runout distances of ejecta due to reduced basal friction and/or enhanced entrainment in atmospheric vortices (see Schultz 1992a), armored surfaces created by thermally indurated soil (melting and migration of subsurface water), and pedestal craters (winds/heat form a crater-centered erosion-resistant surface layer). Here we focus on one particular surface expression, the pedestal crater.

Pedestal Craters

Pedestal craters were first recognized on Mars in Mariner 9 data (McCauley 1973). For our purposes, they are defined as impact craters centered on a plateau or mesa surrounded by a well-defined outward-facing scarp. In some cases, the scarp height can exceed the depth of the crater (Fig. 9). This working definition excludes the craters on Ganymede previously described as pedestal craters (e.g., Horner and Greeley 1982), which actually represent thick continuous ejecta facies, not erosional relics surrounded by scarps. Although there are some differences in usage of the term "pedestal crater," there is a general acceptance that these features are signatures of near-surface volatiles (Mouginis-Mark 1987; Schultz 1988b, 2003; Schultz and Lutz 1988; Thomson and Schultz 2004; Barlow 2005).

Pedestal craters on Mars are concentrated at high latitudes (Amazonian to Late Hesperian in age, see Fig. 9) and in thick equatorial mantling deposits (Early Hesperian to Noachian in age) (Schultz and Lutz 1988). The average diameter of the central crater of pedestal craters at high latitudes is significantly smaller than those in the thick eroded sequences of Arabia and Mesogaea at low latitudes (Schultz 1988b; Schultz and Lutz 1988).

Proposed mechanisms for the formation of pedestal craters include armoring by fine ejecta deposits (Arvidson et al. 1976), ejecta covering a volatile-rich substrate (Schultz and Lutz 1988), and vapor blasts modifying wind-sensitive, volatile-rich substrates (Schultz 1988b, 1992a, 1992b). The recently discovered evidence for volatiles at high latitudes (Boynton et al. 2002) supplies foundation for testing these alternative hypotheses using numerical computations.

A combined atmospheric blast/thermal model as described in this study provides a basis for better understanding the formation of Martian pedestal craters by creating a crater-centered, erosion-resistant indurated surface. Such a model involves processes affecting only the upper surface, consistent with the presence of volatile-rich mantling deposits at high latitudes. "Preconditioning" by the wind blast

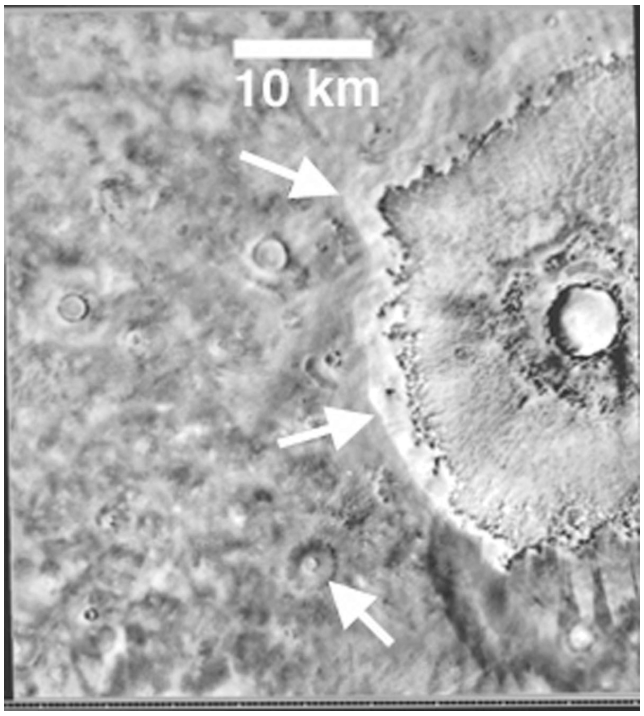

Fig. 9. Image of a Martian pedestal crater ~6 km in diameter located at approximately 75°N, 283°W. Pedestal extends out to ~4 crater diameters. Top two arrows point out the surrounding scarp that is distinctive of high-latitude pedestal craters on Mars. The bottom arrow points out a much smaller example of a pedestal crater. The higher relief pedestal may have formed under very different climate conditions in the past, when much thicker volatile-rich layers were being deposited. The smaller pedestal could have formed during more recent orbital forcing conditions.

would leave a surface scoured and stripped of loose particulates (out to distal distances of several crater diameters, depending on the initial kinetic energy of impact). This, in turn, would make the volatile-rich surface deposits extremely sensitive to the high atmospheric temperatures that immediately follow passage of the blast.

Armoring of the surface surrounding an impact can develop from several possible processes. Two are proposed here. First, melting and migration of near-surface water may indurate soil by rapidly dissolving and precipitating salts. Second, the blast and thermal effects may combine to remove the volatile fraction, leaving behind a protective layer of fine, volatile-poor dust. The consequent striated, armored surface, such as seen around the freshest high-latitude craters (Fig. 1), would be more resistant to erosion than the unaffected volatile-rich deposits farther out. During different climate conditions (in response to orbital forcing or other processes), the breakdown and removal of the volatile-rich component would leave a plateau elevated above the surrounding deflated surface. In some cases, there may be multiple phases of deposition (due to subsequent impacts) followed by exposure, resulting in smaller pedestal craters forming on top of larger pedestals (see Thomson and Schultz 2004).

CONCLUDING REMARKS

Even the tenuous atmosphere of Mars will be affected by an impact in a variety of ways. This study focused on one particular early-time atmospheric response. A more comprehensive investigation of the atmospheric effects observed here will involve further detailed modeling (some laboratory-scale), benchmarked by experiments. Such work is essential for understanding the consequent expressions of these effects (both surface and atmospheric), such as the circulation patterns generated from the chaotic, lingering atmospheric blast-winds. It also establishes the environment for the later stages of impact and ejecta emplacement (e.g., Barnouin-Jha and Schultz 1998). Future studies will explore these topics in greater detail in order to provide a more "complete picture" of atmospheric interactions occurring during an impact.

Acknowledgments–The authors would like to thank O. Barnouin-Jha and E. Asphaug for their constructive comments in review of this manuscript. We also acknowledge the organizers of the Workshop on the Role of Volatiles and Atmospheres on Martian Impact Cratering and the Mars Program Office for providing travel funding to participate. This material is based on work supported by a NASA-Rhode Island Space Grant Graduate Student Fellowship and NASA Grant No. NAG5-11538.

Editorial Handling—Dr. A. J. Timothy Jull

REFERENCES

Adushkin V. V. and Nemchinov I. V. 1994. Consequences of impacts of cosmic bodies on the surface of the Earth. In *Hazards due to comets and asteroids*, edited by Gehrels T., Matthews M. S., and Schumann A. Tucson, Arizona: The University of Arizona Press. pp. 721–778.

Ahrens T. J. and O'Keefe J. D. 1987. Impact on the Earth, ocean and atmosphere. *International Journal of Impact Engineering* 5:13–32.

Arvidson R. E., Coradini M., Carusi A., Coradini A., Fulchignoni M., Federico C., Funiciello R., and Salomone M. 1976. Latitudinal variation of wind erosion of crater ejecta deposits on Mars. *Icarus* 27:503–516.

Arvidson R. E., Guinness E., and Lee S. 1979. Differential aeolian redistribution rates on Mars. *Nature* 278:533–535.

Barlow N. G. 2005. Martian impact craters as revealed by MGS and Odyssey (abstract #1415). 36th Lunar and Planetary Science Conference. CD-ROM.

Barnouin-Jha O. S. and Schultz P. H. 1996. Ejecta entrainment by impact-generated ring vortices: Theory and experiments. *Journal of Geophysical Research* 101:21099–21115.

Barnouin-Jha O. S. and Schultz P. H. 1998. Lobateness of impact ejecta deposits from atmospheric interactions. *Journal of Geophysical Research* 103:25,739–25,756.

Boynton W. B., Feldman W. C., Squyres S. W., Prettyman T. H., Brückner J., Evans L. G., Reedy R. C., Starr R., Arnold J. R., Drake D. M., Englert P. A. J., Metzger A. E., Mitrofanov I., Trombka J. I., d'Uston C., Wänke H., Gasnault O., Hamara D. K.,

Janes D. M., Marcialis R. L., Maurice S., Mikheeva I., Taylor G. J., Tokar R., and Shinohara C. 2002. Distribution of hydrogen in the near surface of Mars: Evidence for subsurface ice deposits. *Science* 297:81–84.

Crawford D. A., Boslough M. B., Trucano T. G., and Robinson A. C. 1995. The impact of periodic comet Shoemaker-Levy 9 on Jupiter. *International Journal of Impact Engineering* 17:253–262.

Crawford D. A., Taylor P. A., Bell, R. L., and Hertel E. S. 2002. Adaptive mesh refinement in the CTH shock physics hydrocode. Proceedings, International Workshop on New Models and Hydrocodes for Shock Wave Processes in Condensed Matter.

Croft S. K. 1985. The scaling of complex craters. Proceedings, 15th Lunar and Planetary Science Conference. *Journal of Geophysical Research* 90:C828–C842.

Greeley R., Lancaster N., Lee S., and Thomas P. 1992. Martian aeolian processes, sediments, and features. In *Mars*, edited by Kieffer H. H., Jakosky B. M., Snyder C. W., and Matthews M. S. Tucson, Arizona: The University of Arizona Press. pp. 730–766.

Holsapple K. A. and Schmidt R. M. 1987. Point source solutions and coupling parameters in cratering mechanics. *Journal of Geophysical Research* 92:6350–6376.

Horner V. M. and Greeley R. 1982. Pedestal craters on Ganymede. *Icarus* 51:549–562.

Jones E. and Kodis J. W. 1982. Atmospheric effects of large body impacts: The first few minutes. In *Geological implications of impact of large asteroids and comets on the Earth*, edited by Silver L. T. and Schultz P. H. Boulder, Colorado: Geological Society of America. pp. 103–120.

McCauley J. F. 1973. Mariner 9 evidence for wind erosion in the equatorial and mid-latitude regions of Mars. *Journal of Geophysical Research* 78:4123–4137.

McGlaun J. M., Thompson S. L., and Elrick M. G. 1990. CTH: A three-dimensional shock wave physics code. *International Journal of Impact Engineering* 10:351–360.

Mouginis-Mark P. J. 1987. Water or ice in the Martian regolith? Clues from rampart craters seen at very high resolution. *Icarus* 71:268–286.

Mustard J. F., Cooper C. D., and Rifkin M. K. 2001. Evidence for recent climate change on Mars from the identification of youthful near-surface ground ice. *Nature* 412:411–414.

Nemtchinov I. V., Popova O. P., Shuvalov V. V., and Svetsov V. V. 1994. Radiation emitted during the flight of asteroids and comets through the atmosphere. *Planetary and Space Science* 42:491–506.

Nemtchinov I. V., Shuvalov V. V., and Greeley R. 2002. Impact-mobilized dust in the Martian atmosphere. *Journal of Geophysical Research* 107, doi:10.1029/2001JE001834.

O'Keefe J. D. and Ahrens T. J. 1982. The interaction of the Cretaceous/Tertiary extinction bolide with the atmosphere, ocean, and solid Earth. In *Geological implications of large asteroids and comets on the Earth*, edited by Silver L. T. and Schultz P. H. Boulder, Colorado: Geological Society of America. pp. 103–120.

Paterson W. B. 1994. *The physics of glaciers*, 3rd ed. New York: Pergamon Press. 250 p.

Pierazzo E. and Melosh H. J. 1999. Hydrocode modeling of Chicxulub as an oblique impact event. *Earth and Planetary Science Letters* 165:163–176.

Roddy D. J., Shuster S., Rosenblatt M., Grant L., Hassig P., and Kreyenhagen K. 1987. Computer simulations of large asteroid impacts into ocean and continental sites preliminary results on atmospheric, cratering and ejecta dynamics. *International Journal of Impact Engineering* 5:123–135.

Rybakov V. A., Nemtchinov I. V., Shuvalov V. V., Artemiev V. I., and Medveduk S. A. 1997. Mobilization of dust on the Mars surface by the impact of small cosmic bodies. *Journal of Geophysical Research* 102:9211–9220.

Schmidt R. M. and Holsapple K. A. 1982. Estimates of crater size for large-body impact: Gravity-scaling rules. In *Geological implications of large asteroids and comets on the Earth*, edited by Silver L. T. and Schultz P. H. Boulder, Colorado: Geological Society of America. pp. 93–102.

Schultz P. H. 1988a. Cratering on Mercury: A relook. In *Mercury*, edited by Villas F., Chapman C., and Matthews M. Tucson, Arizona: The University of Arizona Press. pp. 274–335.

Schultz P. H. 1988b. Impact vaporization of volatile-rich targets: Experimental results and implications (abstract). 19th Lunar and Planetary Science Conference. pp. 1039–1040.

Schultz P. H. 1992a. Atmospheric effects on ejecta emplacement. *Journal of Geophysical Research* 97:11623–11662.

Schultz P. H. 1992b. Atmospheric effects on ejecta emplacement and crater formation on Venus from Magellan. *Journal of Geophysical Research* 97:16,183–16,248.

Schultz P. H. 1996. Effect of impact angle on vaporization. *Journal of Geophysical Research* 101:21,117–21,136.

Schultz P. H. 2003. Impacts into porous volatile-rich substrates on Mars (abstract #3263). The Sixth International Conference on Mars. CD-ROM.

Schultz P. H. and Gault D. E. 1979. Atmospheric effects on Martian ejecta emplacement. *Journal of Geophysical Research* 84:7669–7687.

Schultz P. H. and Gault D. E. 1982. Impact ejecta dynamics in an atmosphere: Experimental results and extrapolations. In *Geological implications of impact of large asteroids and comets on the Earth*, edited by Silver L. T. and Schultz P. H. Boulder, Colorado: Geological Society of America. pp. 153–174.

Schultz P. H. and Gault D. E. 1985. Clustered impacts: Experiments and implications. *Journal of Geophysical Research* 90:3701–3732.

Schultz P. H. and Gault D. E. 1990. *Prolonged global catastrophes from oblique impacts*. Boulder, Colorado: Geological Society of America. pp. 239–261.

Schultz P. H. and Lutz A. B. 1988. Polar wandering of Mars. *Icarus* 73:91–141.

Sedov L. I. 1959. *Similarity and dimensional methods in mechanics*, 10th ed. New York: Academic Press. 479 p.

Stewart S. T., Ahrens T. J., and O'Keefe J. D. 2004. Impact-induced melting of near-surface water ice on Mars. *AIP Conference Proceedings* 706:1484–1487.

Sugita S. and Schultz P. H. 2002. Initiation of runout flows on Venus by oblique impacts. *Icarus* 155:265–284.

Sugita S., Schultz P. H., and Adams M. A. 1998. Spectroscopic measurements of vapor clouds due to oblique impacts. *Journal of Geophysical Research* 103:19,427–19,441.

Tanaka K. L. 2000. Dust and ice deposition in the Martian geologic record. *Icarus* 144:254–266.

Taylor G. 1950a. The formation of a blast wave by a very intense explosion. I. Theoretical discussion. *Proceedings of the Royal Society of London* 201:159–174.

Taylor G. 1950b. The formation of a blast wave by a very intense explosion. II. The atomic explosion of 1945. *Proceedings of the Royal Society of London* 201:175–186.

Thomson B. J. and Schultz P. H. 2004. Erosion rates at the Viking 2 landing site (abstract #1885). 35th Lunar and Planetary Science Conference. CD-ROM.

Wrobel K. E., Schultz P. H., and Heineck J. T. 2004. Non-ballistic vapor-driven ejecta (abstract #1800). 35th Lunar and Planetary Science Conference. CD-ROM.